Supplemental Material of "Designing Multifunctionality via Assembling Dissimilar Materials: Epitaxial AlN/ScN Superlattices"

Zhijun Jiang,[1,2,3,4] Charles Paillard,[3,5] David Vanderbilt,[6] Hongjun Xiang,[1,2,*] and L. Bellaiche[3,†]

[1]*Key Laboratory of Computational Physical Sciences (Ministry of Education), State Key Laboratory of Surface Physics, and Department of Physics, Fudan University, Shanghai 200433, China*

[2]*Collaborative Innovation Center of Advanced Microstructures, Nanjing 210093, China*

[3]*Physics Department and Institute for Nanoscience and Engineering, University of Arkansas, Fayetteville, Arkansas 72701, USA*

[4]*School of Physics and Optoelectronic Engineering, Ludong University, Yantai 264025, China*

[5]*Laboratoire SPMS, CentraleSupélec/CNRS UMR 8580, Université Paris-Saclay, 8-10 rue Joliot Curie, 91190 Gif-sur-Yvette, France*

[6]*Department of Physics and Astronomy, Rutgers University, Piscataway, New Jersey 08854, USA*

The goals of this Supplemental Material (SM) are to provide additional details about (i) computational details; (ii) AlN bulk in its wurtzite form (to be donated as w-AlN) and ScN bulks in their layered hexagonal and rocksalt forms (to be coined h-ScN and r-ScN, respectively); (i-ii) some properties of 1×1 AlN/ScN superlattices; and (iv) some quantities of 1×3 AlN/ScN superlattices.

I. Computational details

We employed the ABINIT package [1] with the local density approximation (LDA) to the density functional theory (DFT) and norm-conserving pseudopotentials [2], chosen in part to facilitate the computation of electro-optic coefficients [3, 4]. We also chose a $6 \times 6 \times 4$ grid of special **k** points and a plane-wave kinetic energy cutoff of 50 Hartree. Both the lattice parameters and the atomic positions of all studied bulk structures were fully relaxed until the force acting on each atom is smaller than 5×10^{-5} Hartree/Bohr. Our DFT calculations are found to (reasonably) underestimate the lattice constants of ScN rocksalt by about 1.33% and of AlN wurtzite by about 0.23%, which can be thought to be indicative that our present results should underestimate the lattice parameters of 1×1 AlN/ScN by about $(1.33\%+0.23\%)/2$ that is close to 0.78%. Note also that our LDA calculations predict a Γ–Γ (direct) band gap of AlN wurtzite of 4.034 eV [see Fig. S1(a)] and a Γ–X (indirect) band gap of rocksalt ScN of -0.21 eV [see Fig. S1(b)]. The comparison between the corresponding experimental values of 6.089 eV [5] and 0.9 ± 0.1 eV [6] allows us to estimate that our LDA band gaps should underestimate the experimental values by about $\{(6.089 - 4.034)/2 + (0.9 + 0.21)/2\}$ which is about 1.58 eV in the 1×1 AlN/ScN superlattices. In addition, we used the hybrid HSE functional to calculate the band gap of wurtzite AlN and rocksalt ScN. The predicted HSE direct Γ–Γ band gap for wurtzite AlN is 5.522 eV [see Fig. S1(c)] and the predicted HSE indirect Γ–X band gap for rocksalt ScN is 0.809 eV [see Fig. S1(d)]. Both values are in good agreement with the experimental values for wurtzite AlN (direct Γ–Γ band gap of 6.089 eV) and rocksalt ScN (indirect Γ–X band gap of 0.9 ± 0.1 eV). We also calculated the band gap for the 1×1 AlN/ScN superlattices using the HSE functional and compared it with the LDA corrected results, that is the band gap of LDA shifted upward by 1.58 eV. Figure S2 compares the HSE band gap with the LDA corrected results in the 1×1 AlN/ScN superlattices, as a function of strain. A rather good agreement can be clearly seen, therefore demonstrating that the correction for the LDA results appears to be valid.

Furthermore, the in-plane lattice vectors were kept fixed while the out-of-plane lattice vector was allowed to relax for epitaxially strained superlattices. The electrical polarization was computed using the Berry phase formalism [7] while phonons, the $S_{33}^{\rm epi}$ elastic compliance element (note that $S_{33}^{\rm epi} = 1/C_{33}$ with the in-plane lattice constants being held fixed) and e_{ij} piezoelectric stress coefficients were calculated using the density functional perturbation theory (DFPT) [8–10]. The $d_{ij}^{\rm epi}$ piezoelectric strain coefficient was obtained by computing $dP_i/d\sigma_j$ [9, 10], where P_i is the i-component of the polarization and σ_j are elements of the stress tensor (in Voigt notations), using finite difference and keeping frozen the in-plane lattice vectors for any investigated strain. For instance, stresses σ_3 were varied by $\pm$0.01 GPa for different epitaxial strains, while the out-of-plane lattice parameter and ionic positions were then relaxed to obtain the polarization P_3. The piezoelectric coefficient $d_{33}^{\rm epi}$ were then obtained from finite difference of polarization with respect to stresses. Elasto-optic coefficients were also calculated from finite difference: strains were typically varied by $\pm$0.001 with respect to their equilibrium values, and ionic positions were then relaxed to obtain the electronic dielectric tensor. The change of the inverse dielectric matrix with respect to strain also allows to obtain the elasto-optic tensor p_{ij} (in Voigt notation).

II. Some properties of w-AlN, h-ScN and r-ScN bulks

Table SI reports structural parameters and band gap E_g of w-AlN, h-ScN and r-ScN bulks, as predicted by our local density approximation (LDA) calculations.

III. Some properties of the 1×1 AlN/ScN superlattices

The presently investigated 1×1 AlN/ScN superlattices have hexagonal parent compounds AlN and ScN, and possess the primitive lattice vectors of the direct Bravais lattice [11, 12] in their relaxed form:

$$\begin{aligned} \mathbf{a}_1 &= a\left(\frac{1}{2}\mathbf{x} - \frac{\sqrt{3}}{2}\mathbf{y}\right), \\ \mathbf{a}_2 &= a\left(\frac{1}{2}\mathbf{x} + \frac{\sqrt{3}}{2}\mathbf{y}\right), \\ \mathbf{a}_3 &= c\mathbf{z}, \end{aligned} \tag{1}$$

where a and c are the in-plane and out-of-plane lattice parameters, respectively. c/a is the axial ratio. The unit vectors along the Cartesian axes are denoted as $\mathbf{x}$, $\mathbf{y}$ and $\mathbf{z}$. The primitive unit cell for 1×1 AlN/ScN superlattices contains four atoms: atoms Sc and Al located at $\mathbf{r}_1$ and $\mathbf{r}_2$, and two N atoms located at $\mathbf{r}_3$ and $\mathbf{r}_4$, with

$$\begin{aligned}
\mathbf{r}_1 &= 0, \\
\mathbf{r}_2 &= \frac{2}{3}\mathbf{a}_1 + \frac{1}{3}\mathbf{a}_2 + \frac{1}{2}\mathbf{a}_3, \\
\mathbf{r}_3 &= u_{\text{ScN}}\mathbf{a_3}, \\
\mathbf{r}_4 &= \frac{2}{3}\mathbf{a}_1 + \frac{1}{3}\mathbf{a}_2 + \left(\frac{1}{2} + u_{\text{AlN}}\right)\mathbf{a}_3.
\end{aligned} \tag{2}$$

The unit cell for the 1×1 AlN/ScN superlattices therefore consists of one layer of AlN being stacked on top of one layer of ScN along the [0001] direction. Note that these ordered structures can be thought as exhibiting two different kinds of u parameter [see Eq. (2)]: the ones connecting the Sc and N atoms that are nearest neighbors along the c-axis and that are denoted by u_{ScN}, *versus* the one binding Al ions and their closest N atoms along $\mathbf{a}_3$ and that is referred to as u_{AlN}.

Once the original superlattices are built, strain is imposed to the vectors $\mathbf{a}_1^* = (1 + \eta_{\text{in}})\mathbf{a}_1$ and $\mathbf{a}_2^* = (1 + \eta_{\text{in}})\mathbf{a}_2$. Meanwhile, the third vector $\mathbf{a_3}$ of the superlattices is allowed to relax as a response to the in-plane strain η_{in}. Note that the zero strain ($\eta_{\text{in}} = 0$) in the 1×1 AlN/ScN superlattices corresponds to the equilibrium structure that is found to be h-derived.

Furthermore, Fig. S3(a) reveals that, near -1.8% (which is the boundary between Regions II and III of the main text), an anticrossing between two modes of identical symmetry occurs, namely between the $A_1^{(1)}$ and $A_1^{(2)}$ modes (that are represented in black and red circles). Such anticrossing is evidenced by the frequencies of these two modes repelling each other but also by the eigenvectors of these two modes inverting their atomic character before *versus* after this anticrossing [see Figs. S3(b) and S3(c) versus S3(d) and S3(e)]. For instance, Al and the N_1 nitrogen atom move in antiparallel fashion along the z-axis in the $A_1^{(1)}$ mode for -1.2% and in the $A_1^{(2)}$ mode for $\eta_{\text{in}} = -1.8\%$, while these two ions move in a parallel manner along the z-axis for both the $A_1^{(2)}$ mode for -1.2% and the $A_1^{(1)}$ mode for $\eta_{\text{in}} = -1.8\%$.

Figure S4 shows the electronic band structure for six different strains (that sample Regions I, II, III and IV) in 1×1 AlN/ScN superlattices.

Figure S5 shows the Born effective charges Z_{33}^* of Sc, Al and N ions as a function of strain.

A specific evolutions of the Born effective charges occurs from regions I to IV. For instance, Z^*_{33} of Sc [see Fig. S5(a)] first linearly decreases with strain in region I and then experiences a large change of its values (from 3.88 to 3.27) in Region II, before further slightly decreasing to a value of about 3.09 in Regions III and IV. For the Al ion, Z^*_{33} [see Fig. S5(a)] first linearly increases with compressive strains in Region I and then adopts a similar qualitative trend as Sc in Regions II, III and IV. For the two different N ions, Z^*_{33} [see Fig. S5(b)] shows linear behaviors in the paraelectric Region I versus non-linear increases with strain in the ferroelectric Regions II, III and IV.

In order to evaluate the bond energies, crystal orbital Hamilton population (COHP) calculations are performed by employing the LOBSTER software package [13–15], where the integrated COHP (ICOHP) up to the Fermi level serves as an indicator for the bond energy. The structures for four selected strains and results are indicated in Fig. S6 and Table SII. As the compressive strain increases, the bonds having the largest magnitude of the bond energy are the *initially-in-plane* Sc-N_1 bonds (that have the shortest bond length between Sc and N ions), and the out-of-plane Al-N_3 bonds (that have the shortest bond length between Al and N ions) – which reflects the dissimilarity between Sc and Al ions. Note that the decrease of the out-of-plane Al-N_3 bond energy is much larger than that of the out-of-plane Sc-N_2 bond energy (1.848 eV vs. 0.488 eV) when the compressive strain is increased up to -5%. This agrees with the fact that Al-N can form a stronger covalent bond than Sc-N.

Moreover, the ferroelectricity in 1×1 AlN/ScN superlattices originates from two effects: (1) Al prefers to form four-fold coordinated Al-N covalent bonds by displacing towards one of the out-of-plane N_3 ions, as evidenced by AlN having a polar wurtzite ground state structure; (2) There is a steric effect related to the in-plane Sc-N bonds. As a matter of fact, the in-plane Sc-N (and Al-N) bond lengths are equal to 2.024 Å in the zero-strain paraelectric structure of the 1×1 AlN/ScN superlattices. This suggests that the in-plane Sc-N bonds are compressed since the sum of the Sc^{3+} ionic radius (0.885 Å for the six-fold coordination case) and N^{3-} ionic radius (1.32 Å for the four-fold coordinate case) is about 2.205 Å – while the in-plane Al-N bonds are elongated since the sum of the Al^{3+} ionic radius (0.53 Å for the four-fold coordinate case) and N^{3-} ionic radius is 1.85 Å. Under compressive strain, the in-plane Sc-N bond lengths become even smaller and thus deviate even more from the sum of their ionic radii, and steric effects then occur leading to ferroelectricity (which allows in-plane Sc-N bond lengths to become longer and closer to the sum of the ionic radii after the ferroelectric transition, in order to reduce the Pauli repulsion between the Sc ion and in-plane N ions) [16]. Note that the fact that in-plane Sc-N and Al-N bonds are identical in the

zero-strain paraelectric structure, while the ionic radii of Sc and Al are rather different, reflects the importance of having a layered structure to more easily favor the paraelectric-to-ferroelectric transition.

Furthermore, to understand the optical mode contributing to the large EO coefficient r_{33}, we decomposed the contributions of each mode to the clamped EO coefficient r_{33}^{η} (note that we just show the mode contributing to r_{33}^{η} for regions II-IV in Fig. S7, because they vanish in Region I). The large r_{33}^{η} mainly comes from the $A_1^{(1)}$ polar mode in Region II (see the inset of Fig. S7), while it is the $A_1^{(2)}$ mode that is the main contributor to r_{33}^{η} in Regions III and IV [note that this change in contribution is fully consistent with the anticrossing between these two modes (see Fig. S3)]. It is interesting to realize that the frequency of this $A_1^{(2)}$ mode is rather large at large compressive strain [see Fig. 1(e) of the main text], which according to the last term of Eq. (2) in the main text, explains why r_{33}^{η} is small at large negative strain.

We also checked the full phonon dispersion for all strain range and did not find any instability in the 1×1 AlN/ScN superlattices. Figure S8 shows the full phonon dispersion for four selected strains that include Regions I, II, III and IV.

IV. Some properties of 1×3 AlN/ScN superlattices

The unit cell for the 1×3 AlN/ScN superlattices is made of one layer of AlN alternating with three layers of ScN along the [0001] direction. Note that the 1×3 AlN/ScN superlattices also can be thought of as exhibiting two different kinds of u parameter as 1×1 AlN/ScN superlattices. For instance, the average over all Sc and N atoms that are nearest neighbors along the c-axis is referred to as $\langle u_{\mathrm{ScN}} \rangle$, and the one connecting all the Al and its closest N atoms along the c-axis is denoted by $\langle u_{\mathrm{AlN}} \rangle$.

Let us now present some of our results for other properties of the 1×3 AlN/ScN superlattices as a function of epitaxial strain ranging between $+6\%$ and -8%. We also chose the same technical approach as in the main text, except that we use here a $6 \times 6 \times 2$ grid of special $\mathbf{k}$ points. Figure S9(a) reports the axial ratio c/a as a function of strain. Figure S9(b) shows the out-of-plane electrical polarization P_z versus strain. Figure S9(c) reports the phonon frequencies at the Γ point. Figure S9(d) displays the LDA electronic band gap and LDA direct band gaps at Γ, H and K points. Figures S9(e)-S9(i) show clamped and unclamped electro-optic (EO) coefficients, piezoelectric strain coefficients d_{33}^{epi}, elasto-optic coefficients, and elastic compliance constants S_{33}^{epi}, respectively,

in the 1×3 AlN/ScN superlattices.

The strain-induced behaviors of the properties reported in Figs. S9(a)–S9(i) allow the determination of four different strain regions (denoted Regions I, II, III and IV), as similar to the case of the 1×1 AlN/ScN superlattices reported in the main text. Regions I and IV also correspond to h-derived and w-derived phases, respectively, while Regions III and IV are two intermediate phases too. Region I concerns strain ranging between $+6\%$ and $\sim -3\%$. Region II is polar, as a result of the softening of the lowest A_1 mode around the left border of Region I, and extends between strains ranging between $\sim -3\%$ and $\sim -4.7\%$. In Region II, the LDA-calculated electronic band gap is indirect (Γ-to-K) [see red circle in Fig. S9(d)] and varies from 0.82 to 2.79 eV [the corrected-with-respect-to-LDA value therefore varies from 2.17 to 4.14 eV (since we estimate to underestimate the experimental values by $\{(6.089 - 4.034)/4 + 3 \times (0.9 + 0.21)/4\}$ that is close to 1.35 eV in the 1×3 AlN/ScN superlattices, when comparing and weighting the theoretical and experimental band gaps of w-AlN and r-ScN bulks) which correspond to the electromagnetic spectra covering the yellow color to middle ultraviolet (via green, cyan, blue violet and near ultraviolet)]. As shown in Fig. S9(c) and detailed in Fig. S10, an anticrossing between different A_1 modes occur at -4.7%, which is accompanied with the emergence of Region III that extends to a compressive strain $\sim -5.3\%$. Finally, Region IV occurs for compressive strains smaller than -5.3%, with the boundary between Regions III and IV corresponding to the beginning of the plateau of the electronic band gap [see red circle in Fig. S9(d)]. Note that the band structure for different strains also shown in Fig. S11.

Figure S9 further reveals a lot of striking features related to physical responses such as: (1) polarization P_z increasing from a null value to a giant 1.11 C/m^2 from Regions I to IV; (2) large value of clamped and unclamped EO coefficients r_{33}^{η} and r_{33}^{σ}, respectively, at the boundary between Regions I and II [see Figs. S9(e) and S9(f)]; (3) the piezoelectric coefficient $d_{33}^{\rm epi}$ adopting a large value at $\eta_{\rm in} \sim -3\%$; (4) r_{13}^{σ} exhibiting a kind of a plateau in Region III [see the inset of Fig. S9(f)], which is found to originate from a corresponding plateau in $d_{33}^{\rm epi}$ [see the inset of Fig. S9(g)]; (5) an extremely large value of the elasto-optic coefficient p_{33} [see Fig. S9(h)] at the boundary between Regions I and II, that is twice as large as in $BaTiO_3$ [17] and about 5 times than the 1×1 AlN/ScN superlattices; and (6) the elastic compliance coefficient $S_{33}^{\rm epi}$ of Fig. S9(i) having a maximum at the boundary between Regions II and III.

* hxiang@fudan.edu.cn

† laurent@uark.edu

[1] X. Gonze, J.-M. Beuken, R. Caracas, F. Detraux, M. Fuchs, G.-M. Rignanese, L. Sindic, M. Verstraete, G. Zerah, F. Jollet, M. Torrent, A. Roy, M. Mikami, Ph. Ghosez, J.-Y. Raty, and D. C. Allan, Comput. Mater. Sci. **25**, 478 (2002).

[2] D. R. Hamann, Phys. Rev. B **88**, 085117 (2013).

[3] M. Veithen, X. Gonze, and Ph. Ghosez, Phys. Rev. Lett. **93**, 187401 (2004).

[4] M. Veithen, X. Gonze, and Ph. Ghosez, Phys. Rev. B **71**, 125107 (2005).

[5] M. Feneberg, R. A. R. Leute, B. Neuschl, K. Thonke, and M. Bickermann, Phys. Rev. B **82**, 075208 (2010).

[6] H. A. Al-Brithen, A. R. Smith, and D. Gall, Phys. Rev. B **70**, 045303 (2004).

[7] R. Resta, Rev. Mod. Phys. **66**, 899 (1994).

[8] X. Gonze and C. Lee, Phys. Rev. B **55**, 10355 (1997).

[9] D. R. Hamann, X. Wu, K. M. Rabe, and D. Vanderbilt, Phys. Rev. B **71**, 035117 (2005).

[10] X. Wu, D. Vanderbilt, and D. R. Hamann, Phys. Rev. B **72**, 035105 (2005).

[11] V. Ranjan, S. Bin-Omran, L. Bellaiche, and A. Alsaad, Phys. Rev. B **71**, 195302 (2005).

[12] V. Ranjan, S. Bin-Omran, D. Sichuga, R. S. Nichols, L. Bellaiche, and A. Alsaad, Phys. Rev. B **72**, 085315 (2005).

[13] R. Dronskowski and P. E. Blöchl, J. Phys. Chem. **97**, 8617 (1993).

[14] V. L. Deringer, A. L. Tchougréeff, and R. Dronskowski, J. Phys. Chem. A **115**, 5461 (2011).

[15] S. Maintz, V. L. Deringer, A. L. Tchougréeff, and R. Dronskowski, J. Comput. Chem. **34**, 2557 (2013).

[16] T. Gu, T. Scarbrough, Y. Yang, J. Íñiguez, L. Bellaiche, and H. J. Xiang, Phys. Rev. Lett. **120**, 197602 (2018).

[17] M. Zgonik, P. Bernasconi, M. Duelli, R. Schlesser, P. Günter, M. H. Garrett, D. Rytz, Y. Zhu, and X. Wu, Phys. Rev. B **50**, 5941 (1994).

TABLE SI. LDA structural parameters and band gap E_g of w-AlN, h-ScN and r-ScN

Property	w-AlN	h-ScN	rocksalt ScN
a (Å)	3.117	3.669	4.438
c (Å)	4.986	4.423	4.438
u	0.381	0.5	N/A
Nature of Band gap	Direct (Γ–Γ)	Indirect (Γ–K)	Indirect (Γ–X)
E_g(eV)	4.034	0.25	-0.21

TABLE SII. Bond distance (Å) and energy (eV) of Sc-N and Al-N for four selected strains at 0% (Region I), -1% (Region II), -2% (Region III), and -5% (Region IV).

	Sc-N_2		Sc-N_1		Al-N_3		Al-N_2	
Strain	Distance	Energy	Distance	Energy	Distance	Energy	Distance	Energy
0%	2.155	-2.230	2.024	-3.373	2.155	-3.857	2.024	-4.534
-1%	2.140	-2.404	2.008	-3.520	2.025	-4.667	2.006	-4.659
-2%	2.144	-2.495	2.002	-3.640	1.933	-5.287	1.996	-4.774
-5%	2.131	-2.718	2.003	-3.823	1.887	-5.705	1.975	-4.904

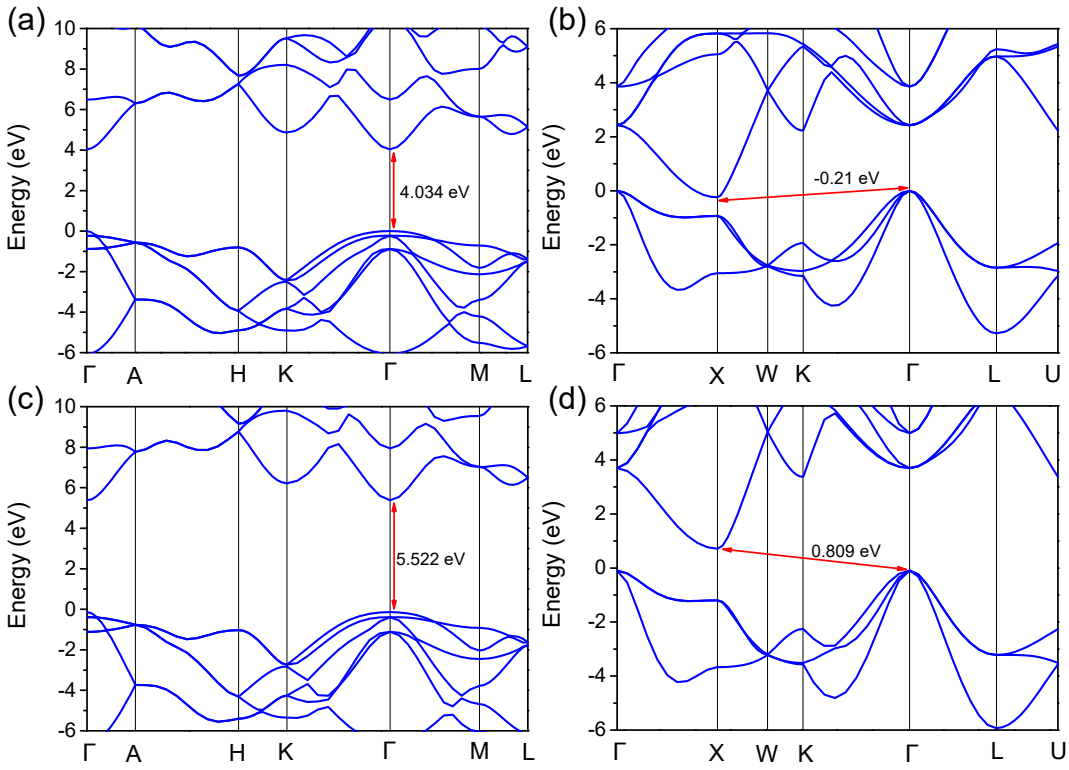

FIG. S1. LDA band structure of (a) wurtzite AlN and (b) rocksalt ScN. HSE band structure of (c) wurtzite AlN and (d) rocksalt ScN.

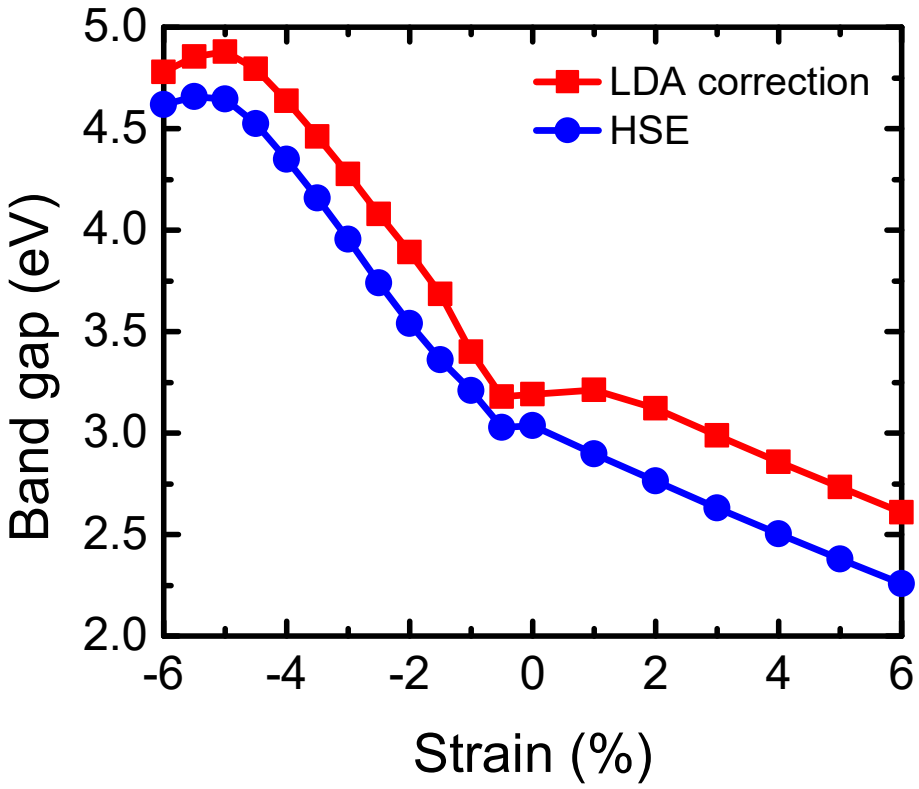

FIG. S2. The band gap with the LDA correction and HSE results in the 1×1 AlN/ScN superlattices as a function of strain.

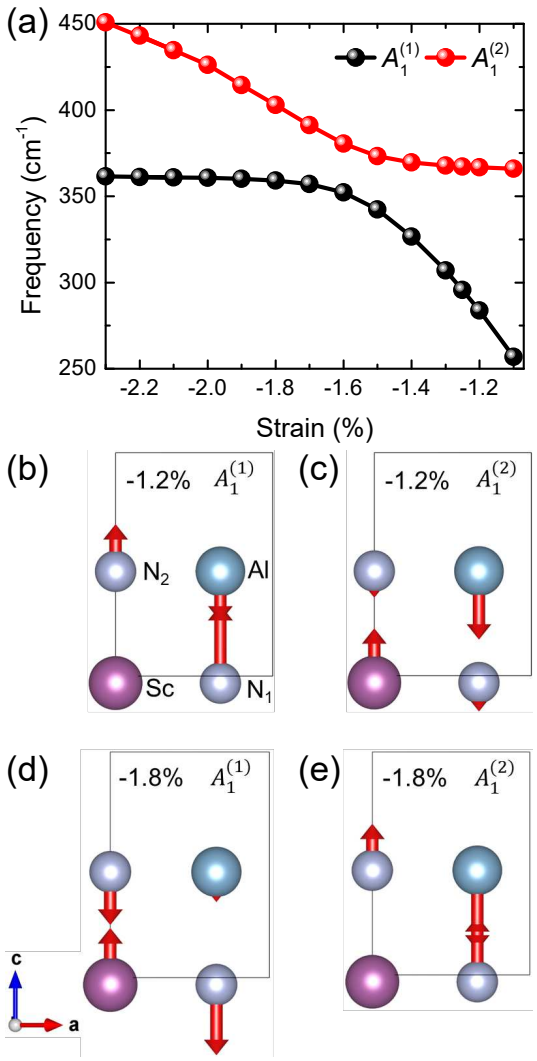

FIG. S3. (a) Frequencies of the $A_1^{(1)}$ and $A_1^{(2)}$ modes for strains ranging between -2.3% and -1.1% in the 1×1 AlN/ScN superlattices. Panels (b), (c), (d) and (e) show the displacement pattern (red arrows) of the eigenvectors of these $A_1^{(1)}$ and $A_1^{(2)}$ modes for strains of -1.2% and -1.8%.

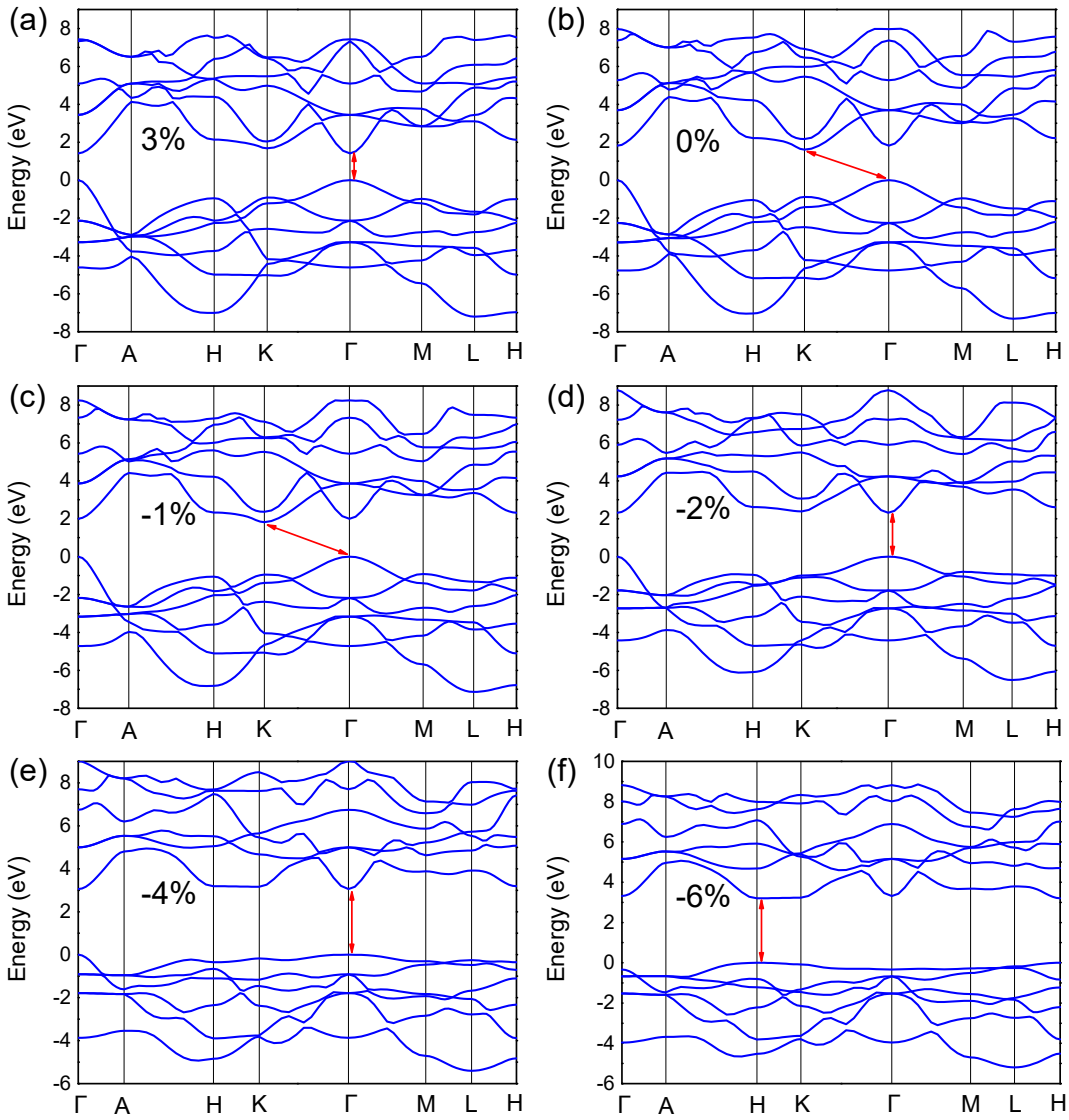

FIG. S4. The electronic band structure of 1×1 AlN/ScN superlattices for six selected strains at (a) 3% (Region I); (b) 0% (Region I); (c) -1% (Region II); (d) -2% (Region III); (e) -4% (Region IV); and (f) -6% (Region IV).

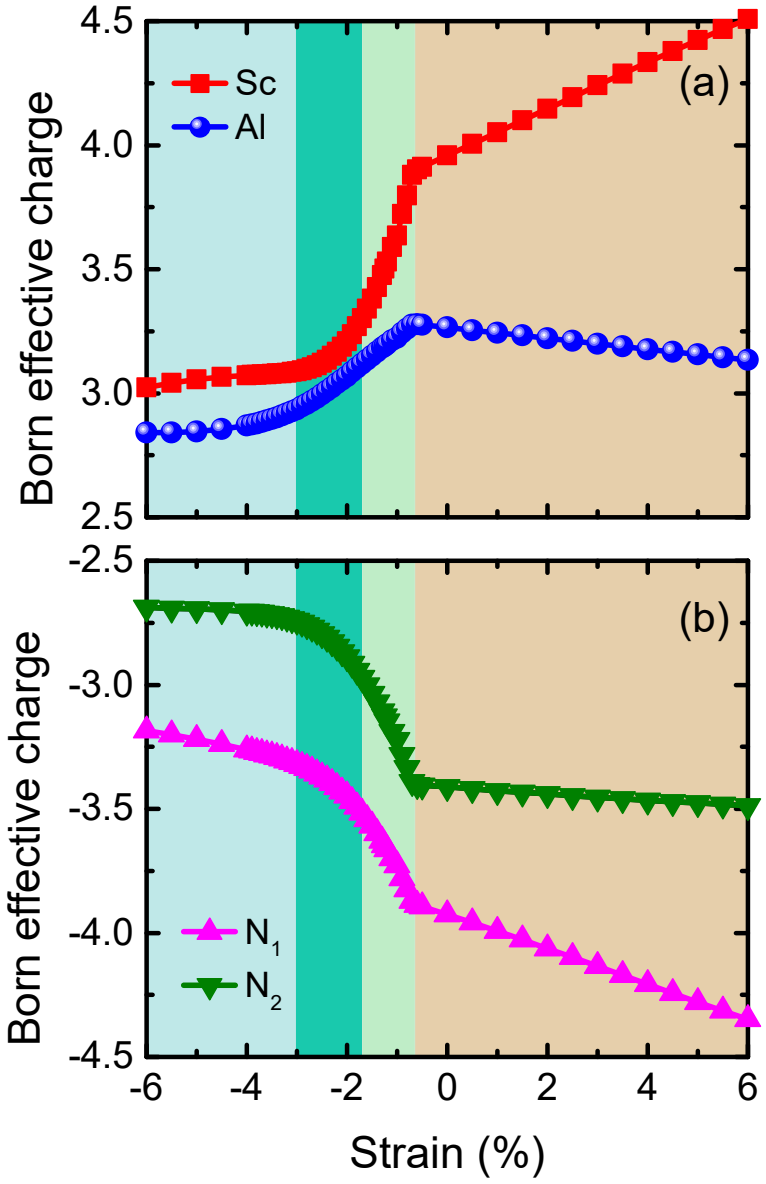

FIG. S5. Born effective charges Z^*_{33} of (a) Sc and Al ions; and (b) the two different types of N ions as a function of strain.

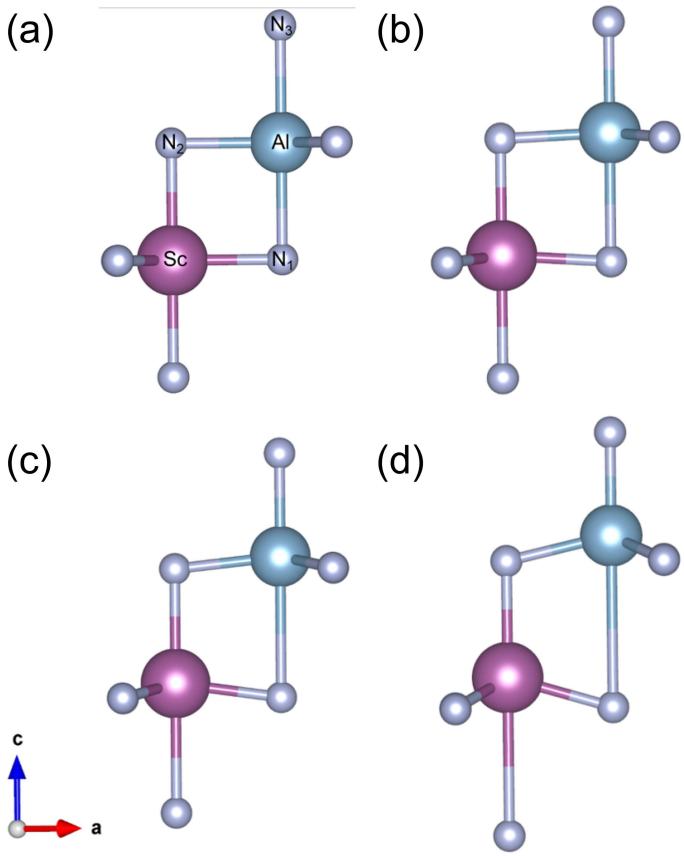

FIG. S6. Crystal structures of the 1×1 AlN/ScN superlattices. Panels (a), (b), (c) and (d) show the strain at 0%, -1%, -2% and -5%.

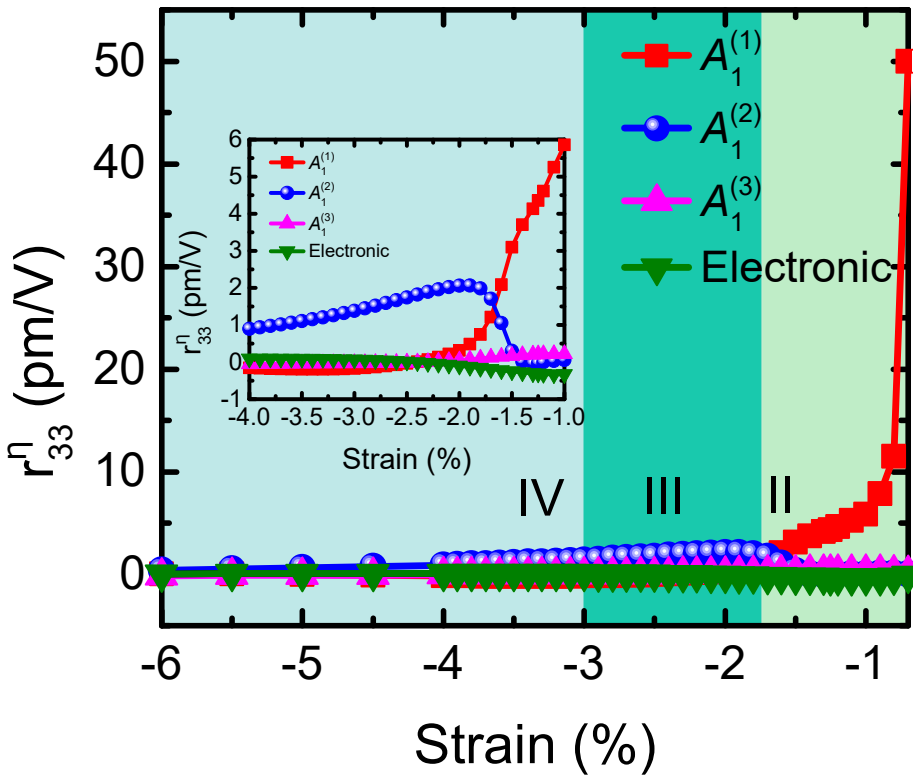

FIG. S7. Mode decompostion of the clamped EO coefficient r_{33}^{η} (the inset zooms in the data for strains between -4% and -1%).

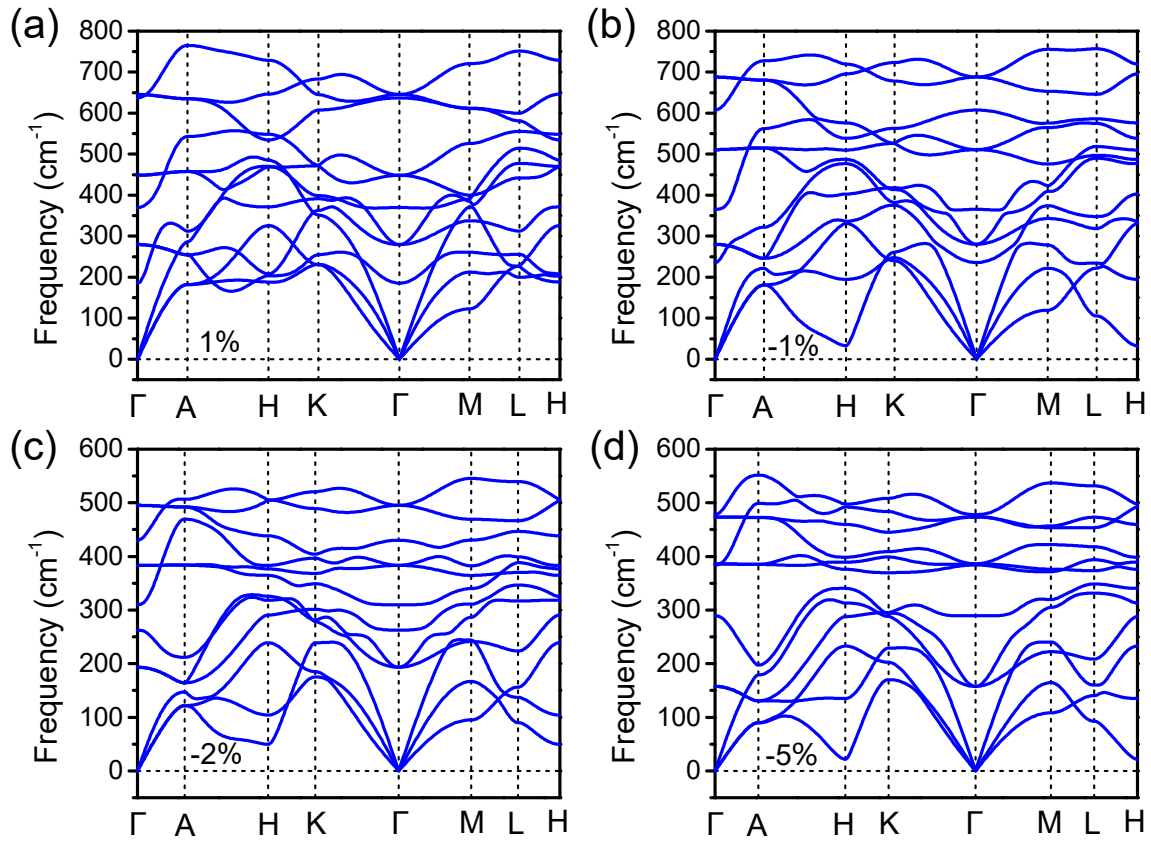

FIG. S8. The full phonon dispersion of the 1×1 AlN/ScN superlattices for four selected strains at (a) 1% (Region I); (b) -1% (Region II); (c) -2% (Region III); and (d) -5% (Region IV).

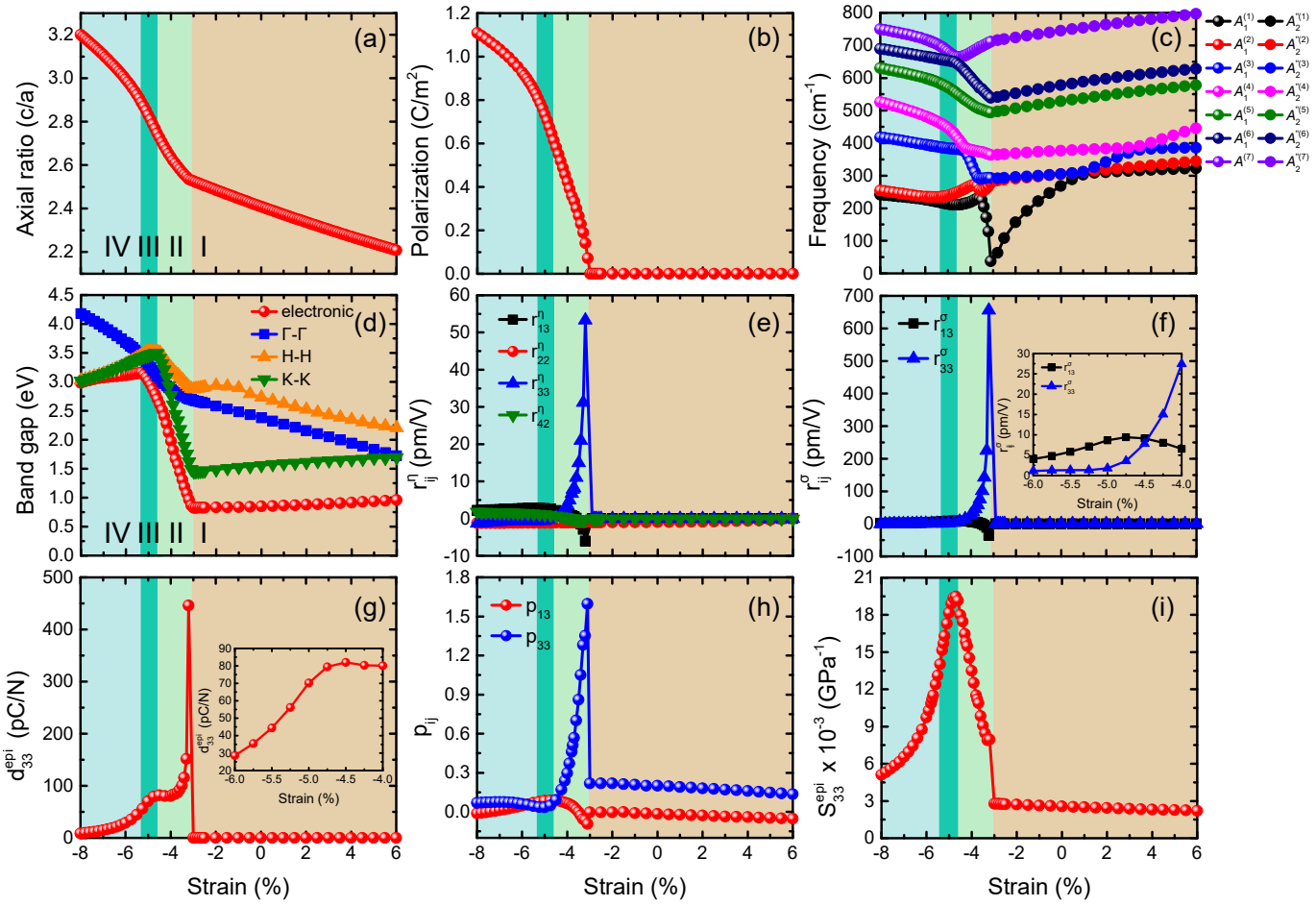

FIG. S9. Evolution with strain of the (a) axial ratio c/a; (b) polarization P_z; (c) phonon spectrum at the Γ point of the first Brillouin zone; (d) the electronic band gap and the direct band gaps at Γ, H and K; (e) clamped electro-optic coefficients; (f) unclamped electro-optic coefficients (the inset zoom in the unclamped electro-optic coefficients data for strains between -6% and -4%); (g) piezoelectric strain coefficients $d_{33}^{\rm epi}$ (the inset zooms in the data for strains between -6% and -4%); (h) elasto-optic coefficients p_{13} and p_{33}; and (i) elastic compliance constants $S_{33}^{\rm epi}$ in the studied 1×3 AlN/ScN superlattices.

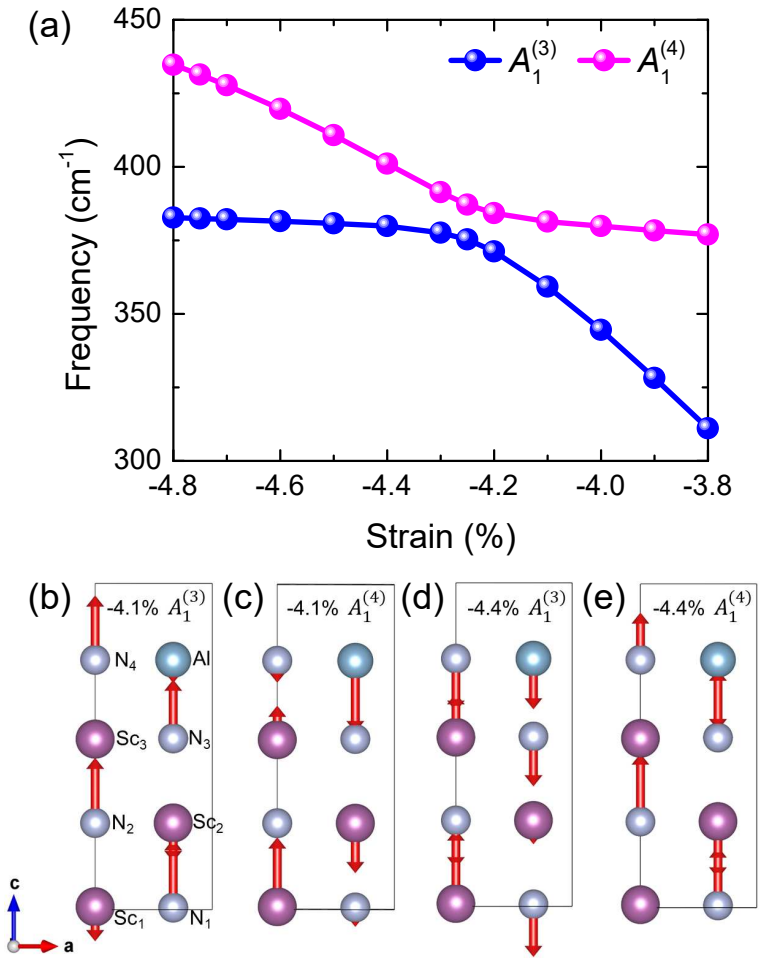

FIG. S10. (a) Frequencies of the $A_1^{(3)}$ and $A_1^{(4)}$ modes for strains ranging between -4.8% and -3.8% in the 1×3 AlN/ScN superlattices. Panels (b), (c), (d) and (e) show the displacement pattern (red arrows) of the eigenvectors of these $A_1^{(3)}$ and $A_1^{(4)}$ modes for strains of -4.1% and -4.4%.

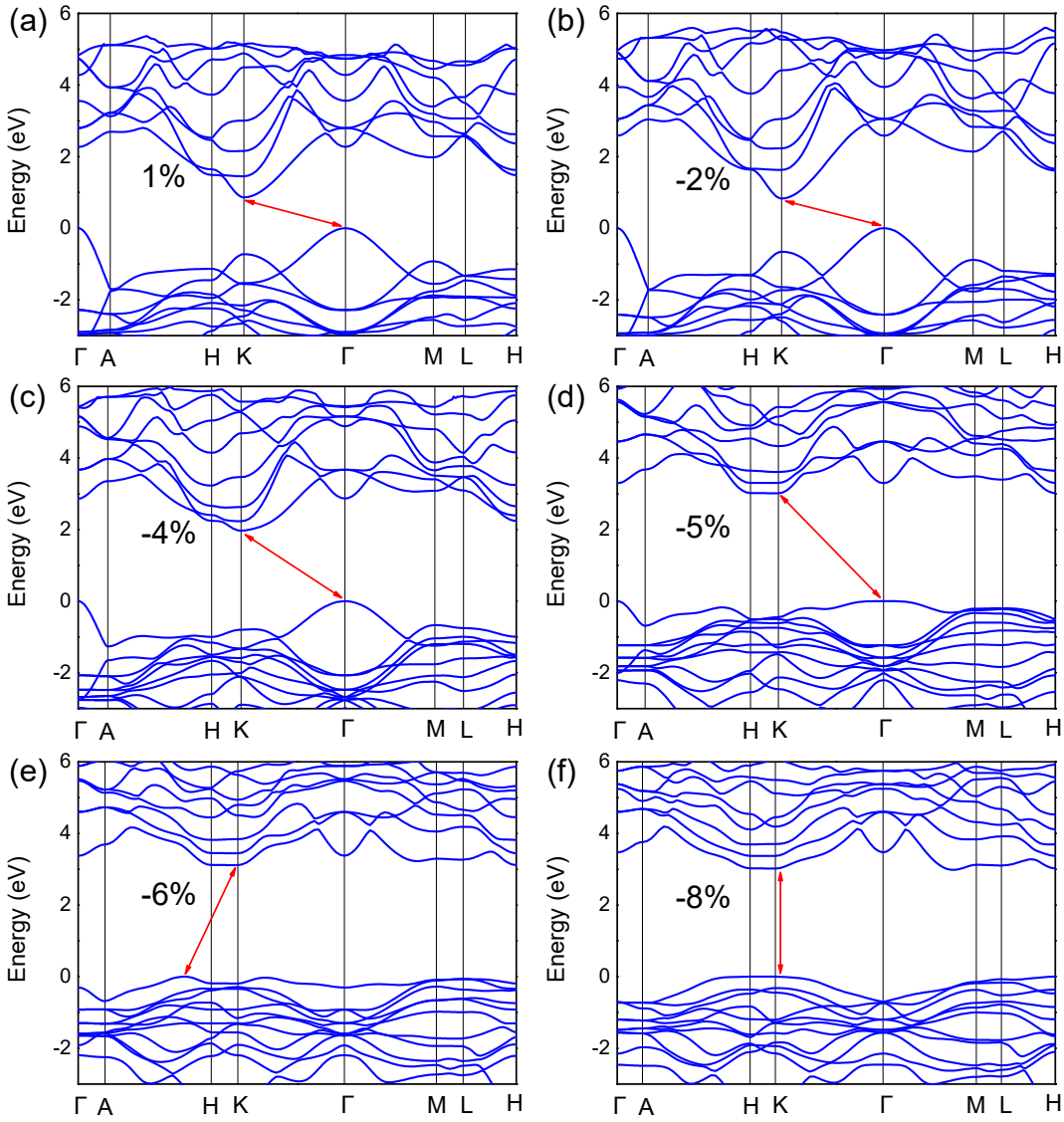

FIG. S11. The band structure of 1×3 AlN/ScN superlattices for six selected strains at (a) 1% (Region I); (b) -2% (Region I); (c) -4% (Region II); (d) -5% (Region III); (e) -6% (Region IV); and (f) -8% (Region IV).